A thermodynamic explanation of the Invar effect

S. H. Lohaus*, ¹ M. Heine*, ² P. Guzman, ¹ C. M. Bernal-Choban, ¹ C. N. Saunders, ¹ G. Shen, ³ O. Hellman, ⁴ D. Broido, ² and B. Fultz ¹

**Dept. of Applied Physics and Materials Science,

**California Institute of Technology, Pasadena, CA 91125, USA

**2Dept. of Physics, Boston College, Chestnut Hill, MA 02467, USA

**3Advanced Photon Source, Argonne National Laboratory, Argonne, IL 60439, USA

**4Dept. of Molecular Chemistry and Materials Science,

**Weizmann Institute of Science, Rehovoth 76100, Israel

(Dated: October 19, 2023)

The anomalously low thermal expansion of Fe-Ni Invar has long been associated with magnetism, but to date, the microscopic underpinnings of Invar behavior have eluded both theory and experiment. Here, we present nuclear resonant X-ray scattering measurements of the phonon and magnetic entropy under pressure. By applying a thermodynamic Maxwell relation to these data, we obtain the separate phonon and magnetic contributions to thermal expansion. We find that the Invar behavior stems from a competition between phonons and spins. In particular, the phonon contribution to thermal expansion cancels the magnetic contribution over the 0-3 GPa pressure range of Invar behavior. At pressures above 3 GPa the cancellation is lost, but our analysis reproduces the positive thermal expansion measured separately by synchrotron X-ray diffractometry. Ab initio calculations informed by experimental data show that spin-phonon interactions improve the accuracy of this cancellation over the range of Invar behavior. Spin-phonon interactions also explain how different phonon modes have different energy shifts with pressure.

INVAR ANOMALY AND ITS INTERPRETATIONS

Invar is a magnetic alloy of iron and nickel with an anomalous near-zero thermal expansion at ambient temperature and pressure. It has long been used in precision instrumentation and mechanical devices that require dimensional stability against changes in temperature [1]. Although the anomalous thermal expansion known as the "Invar effect" was discovered in Fe₆₅Ni₃₅, it has since been found in Fe-Pd, Fe-Pt, and other crystalline and amorphous alloys of iron with transition metals. The 1920 Nobel Prize in physics was awarded to its discoverer, C.E. Guillaume, who realized that the Invar effect is related to magnetism [2, 3]. Curiosity about the role of magnetism in this anomalous thermal expansion has stimulated thousands of studies of the Invar effect and related phenomena.

A general expectation for Invar materials is that magnetism causes a negative thermal expansion coefficient to counteract a positive thermal expansion of the lattice. This magneto-volume effect arises from the rich magnetic landscape of iron, and its dependence on volume and local atomic configurations. In the closed-packed fcc structure, the spin alignment of pure iron varies from anti-ferromagnetic at low volumes to ferromagnetic at larger volumes, as found by ab inito calculations [4, 5] and Mössbauer experiments [6]. Early explanations of the Invar effect proposed a two-state picture, in which a

thermally-induced electronic transition from a high-spin state to a low-spin state with smaller volume was assumed to compensate a conventional thermal expansion [7].

Calculations using local-spin-density approximations predicted different ferromagnetic phases (non-magnetic, high-moment, and low-moment) as a function of volume in fcc Fe [8] and Fe-Ni alloys [9, 10]. These phases coexisted in limited ranges of volume. A microscopic picture of the magneto-volume effect is provided by spinpolarized band calculations: when electrons near the Fermi energy in majority-spin \mathbf{t}_{2g} orbitals are excited into unoccupied minority-spin e_g orbitals, there is a simultaneous reduction of magnetism and volume [10]. More recent ab initio calculations revealed increasingly complex interactions between non-colinear spins [11, 12], with several competing magnetic states and spin arrangements [13], including magnetic short-range order [14]. Temperature complicates the picture by inducing more interactions between electrons, their spins, and coupling with lattice vibrations. Consequently, there is still no widely accepted microscopic model of temperature-dependent magnetism in Invar. Additionally, the appealing explanation of Invar behavior as a magneto-volume effect, where a low-spin state has a smaller atomic volume has not had quantitative success.

Today the electronic structure of Invar is well established [9–11, 13–16], and it is known to change under pressure [17, 18]. Since the volume of Invar depends on magnetism, much research on the Invar effect has focused on electrons and their spins. However, phonons (quantized modes of atom vibrations) play a central role in the thermophysical properties of materials, includ-

^{*} These authors contributed equally.

ing thermal expansion. An early analytical model of Invar behavior was developed with phonons and magnetostriction [19], but accurate treatments of thermal expansion should account for phonon behavior beyond adaptations of harmonic phonons to changes in volume [20]. Computational work on phonons in Fe-Ni alloys indicate an electron-phonon coupling, where phonons may assist the electronic transition from spin-up t_{2g} to spindown e_q states, lowering the frequencies of transverse phonons [9, 21]. More recently, the effects of magnons on phonon energies were studied from first-principles [22]. Phonon instabilities may also be at the core of a structural martensite transformation experienced by Fe-Ni alloys at large Fe concentrations (> 70% Fe) [9, 23]. In this region, the anti-Invar effect is observed, where the thermal expansion is enhanced relative to a non-magnetic crystal [15]. The phonon dispersions in Invar have been measured by inelastic neutron scattering along high symmetry directions [24, 25]. Nevertheless, with few exceptions, the thermal expansion from phonons is missing in explanations of the Invar effect.

Here we use a thermodynamic Maxwell relation to separate explicitly the contributions to thermal expansion from phonons and spins. These two contributions were measured by nuclear resonant X-ray scattering on Invarunder pressure. We find that a competition with phonons is necessary to complete the explanation of the near-zero thermal expansion of Invar. In the range of Invar behavior, our ab initio simulations reveal spin-phonon interactions that improve the accuracy of this cancellation of phonon and spin contributions to thermal expansion.

The volume coefficient of thermal expansion is the fractional change in volume, V, with temperature, T,

$$\beta = \frac{1}{V} \left(\frac{\partial V}{\partial T} \right)_{P} . \tag{1}$$

Equilibration between phonons and spins is far faster than the times of macroscopic measurements of β , so a thermodynamic Maxwell relation

$$\left(\frac{\partial V}{\partial T}\right)_{P} = -\left(\frac{\partial S}{\partial P}\right)_{T} , \qquad (2)$$

allows a rigorous expression of the thermal expansion as

$$\beta = -\frac{1}{V} \left(\frac{\partial S}{\partial P} \right)_T . \tag{3}$$

Phonons, spins, and electrons contribute to the entropy as $S_{\rm ph}$, $S_{\rm mag}$, and $S_{\rm el}$, so the thermal expansion also has contributions from the vibrational, magnetic, and electronic degrees of freedom as

$$\beta = -\frac{1}{V} \left[\left(\frac{\partial S_{\text{ph}}}{\partial P} \right)_T + \left(\frac{\partial S_{\text{mag}}}{\partial P} \right)_T + \left(\frac{\partial S_{\text{el}}}{\partial P} \right)_T \right] . \quad (4)$$

An advantage to Eq. 4 is that the two main components of the thermal expansion, phonon and magnetic, can be

obtained experimentally by nuclear resonant X-ray scattering.

First principles calculations, which explicitly incorporate the temperature and pressure dependencies of lattice and spin sub-systems, and spin-lattice coupling [26, 27], were performed to support the experiments and complete the analysis of Eq. 4. Excellent agreement between experiment and theory is found. There is a remarkable spin-lattice coupling, and a precise cancellation of the phonon and spin contributions that causes the anomalously low thermal expansion in Invar near ambient conditions of T and P. Furthermore, the transition to a more typical thermal expansion at higher pressures is shown to arise from the magnetic transition to the paramagnetic state that quenches the negative contribution from the spin system. Finally, the electronic contribution is found to have only a small effect on the thermal expansion.

MEASUREMENTS

The experiments were performed at sectors 3 and 16 of the Advanced Photon Source (APS) at the Argonne National Laboratory. Details are presented in the Methods section, but suffice to say that the small size of the X-ray beam at the APS allows for measurements on small samples under controlled pressures in diamond anvil cells. To use Eq. 4, the pressure range of Invar behavior must be known. Measurements of lattice parameter versus pressure at two temperatures showed that there is no detectable thermal expansion between room temperature (RT) and 390 K for pressures below 3 GPa (see Fig. 4c and Supplementary Fig. S1). At higher pressures, however, the volume increases with temperature, becoming a more typical $\beta=3.4\cdot 10^{-5}~{\rm K}^{-1}.$

Nuclear forward scattering (NFS) measurements show clear magnetic beats at low pressures. These were fitted to temporal interference patterns of photons emitted from ⁵⁷Fe nuclei with different hyperfine magnetic fields (HMF) [28] (measurements and fits are shown in the Supplementary Figs. S2 and S3). Pressure reduces the HMF, following a decreasing magnetization of the lattice. Phonon spectra were measured at pressures up to 21.3 GPa by nuclear resonant inelastic X-ray scattering (NRIXS), which gives the phonon partial density of states of ⁵⁷Fe atoms [29]. For consistency, NRIXS and NFS spectra were collected sequentially from the same sample under identical experimental conditions. Since these nuclear resonant techniques are sensitive only to ⁵⁷Fe, Invar materials were prepared using this isotope as 57 Fe₆₅Ni₃₅.

THEORY

A challenge in treating Invar from first principles is the lack of an accepted microscopic model for its magnetism. Previous theories [7, 11] postulated mechanisms for the drop in magnetization, but these have been called into question [13, 14]. Here we remain agnostic about the physical mechanism of the magnetic transition, and instead allow experiment to guide the theory. We adopted a hybrid approach that integrates measured magnetization data into the calculations, as detailed in the Methods section. Upon integrating input from experiment, the calculations were performed from first principles. The absence of an accepted model for magnetic interactions including spin-lattice coupling in Invar precluded ab initio calculations of the magnetic entropy.

The calculations were performed at RT within the framework of the Temperature Dependent Effective Potential (TDEP) approach [26, 30, 31]. This method incorporates the renormalization of phonon modes by (i) chemical disorder (i.e. alloys), (ii) temperature and pressure-induced vibrational and magnetic disorder, (iii) spin-lattice coupling, and (iv) local environment effects. Fully non-collinear magnetism with spin-orbit coupling was included [27].

PHONON ENTROPY

The measured phonon densities of states (DOS) shown in Fig. 1 are in excellent agreement with the calculations, as seen by the agreement in the energies of their Van Hove singularities (and in their nearly equal integrated areas between these singularities). The NRIXS technique uses ⁵⁷Fe nuclei to give a partial phonon DOS of the Fe atoms. We measured inelastic neutron scattering (INS) spectra on Fe₆₅Ni₃₅, for which Ni has a 50% larger crosssection than Fe for phonon scattering. INS measurements at ambient conditions were performed with the ARCS instrument at the Spallation Neutron Source of the Oak Ridge National Laboratory (see Methods for details). The neutron-weighted DOS agrees with the Fe partial DOS from the NRIXS measurements (Fig. 1), so both are representative of the true phonon DOS (see Supplementary Fig. S5 for details). The phonon entropy, $S_{\rm ph}$, is determined from the phonon DOS, $g(\varepsilon)$, as [32]:

$$S_{\rm ph} = 3k_{\rm B} \int_0^\infty g(\varepsilon) \left[(1 + n_{\varepsilon,T}) \ln(1 + n_{\varepsilon,T}) - n_{\varepsilon,T} \ln n_{\varepsilon,T} \right] d\varepsilon , \qquad (5)$$

where ε is the phonon energy, and $n_{\varepsilon,T} = (\exp(\varepsilon/k_{\rm B}T) - 1)^{-1}$ is the Planck distribution for phonon occupancy.

Figure 2 shows the agreement between theory and experiment for the pressure-dependent $S_{\rm ph}(P)$. The experimental data between 5.7 and 10.7 GPa have smaller

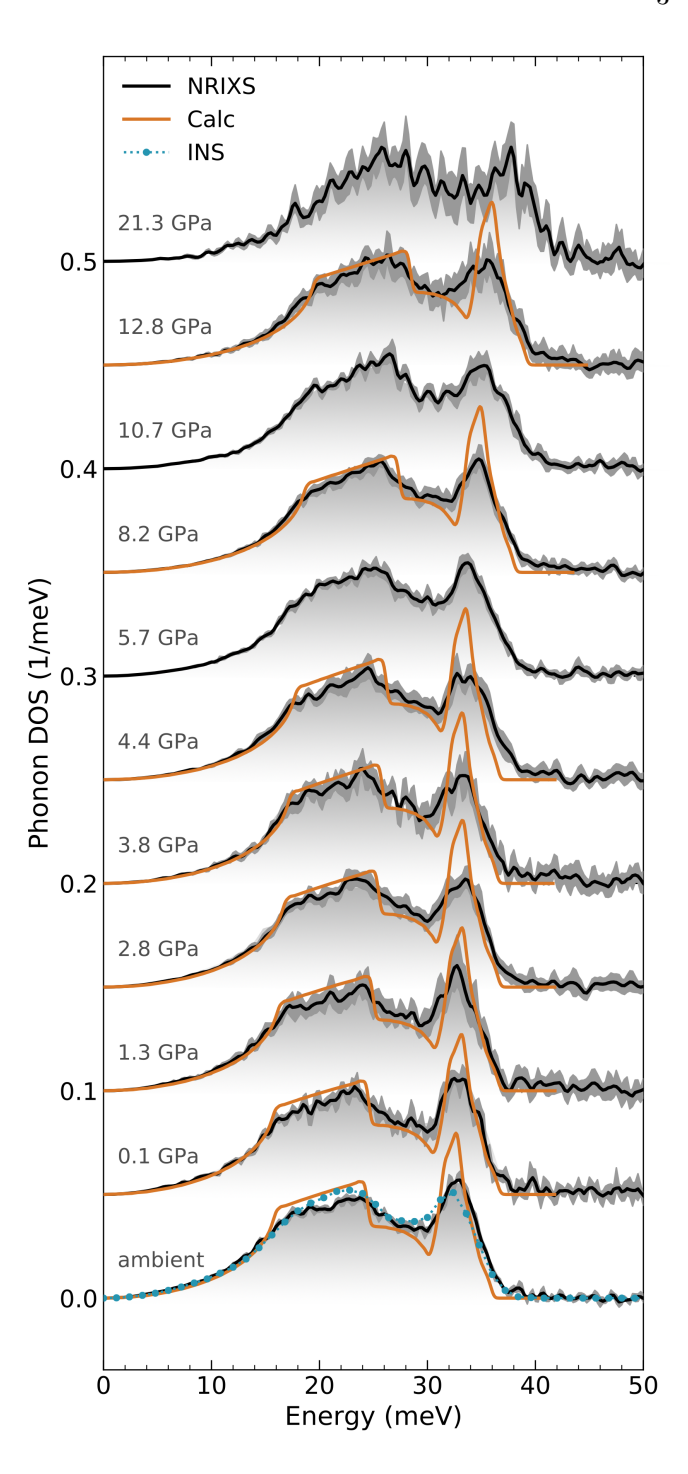


FIG. 1. Phonon DOS of Invar at different pressures as labeled. Experimental partial DOS curves measured by NRIXS (black curves) are compared to the calculated DOS (orange curves), both are normalized to 1. Error bars show the standard deviation of sequential NRIXS scans (on average, a total of 39,480 counts were recorded for each inelastic spectrum). At ambient conditions, the NRIXS measurement is in excellent agreement with the DOS measured by INS (blue markers).

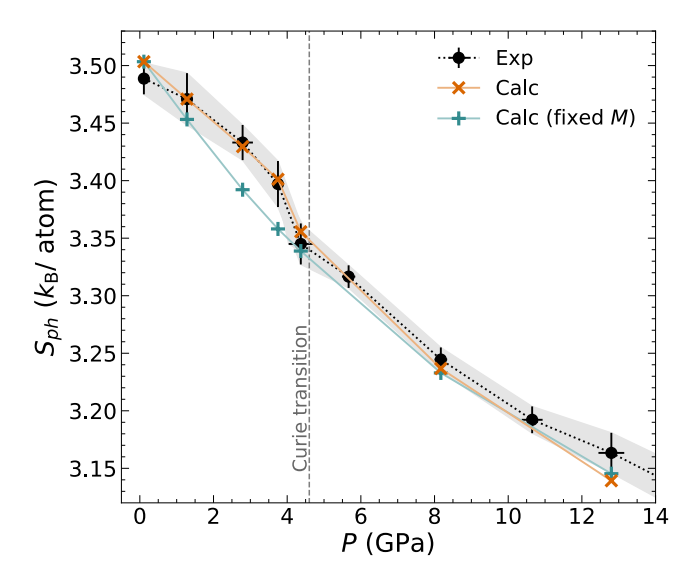


FIG. 2. Phonon entropy of Invar as a function of pressure. The entropy, $S_{\rm ph}(P)$, was calculated with Eq. 5 using the experimental (Exp) and calculated (Calc) phonon density of states. Calc: full calculation using M(P) according to Fig. 3. Calc (fixed M): magnetization artificially fixed at the ambient value. Calculated curves are shifted so their volumes coincide with the experimental at ambient volume. Experimental error bars were propagated from the DOS errors and represent the standard deviation of sequential measurements. They were calculated using Eq. 5 from an ensemble of 200 DOS curves generated from the error bars of Fig. 1 by a Monte-Carlo method. The standard deviation in pressure was computed from two pressure probes (ruby spheres) inside the diamond anvil cell, measured before and after each spectrum (see Methods).

errors because of an improved count rate (see Methods). The experimental and theoretical $S_{\rm ph}(P)$ curves both display a dip near the pressure corresponding to the Curie transition at 4.6 GPa. The calculations are able to reproduce this dip only if the magnetism is allowed to collapse at that pressure. To elucidate the significance of this behavior, we note that the two main mechanisms for the change in $S_{\rm ph}$ with pressure are (i) those that result purely from volume changes, and (ii) those resulting from the pressure-induced changes in magnetization. The hybrid first principles calculations including both effects give the orange curve in Fig. 2. To identify the importance of (ii), we also performed calculations of $S_{\rm ph}$ vs. volume with the magnetization fixed artificially at its value at ambient volume (teal curve in Fig. 2). Near ambient pressure, calculations of $S_{\rm ph}$ that include the pressure-induced reduction in magnetization (orange curve) have approximately a 30% smaller slope. This shows how the disordering of magnetic spins suppresses significantly the change of phonon entropy, and consequently, the phonon contribution to the thermal expansion of Invar through Eq. 4. Spin-lattice coupling plays,

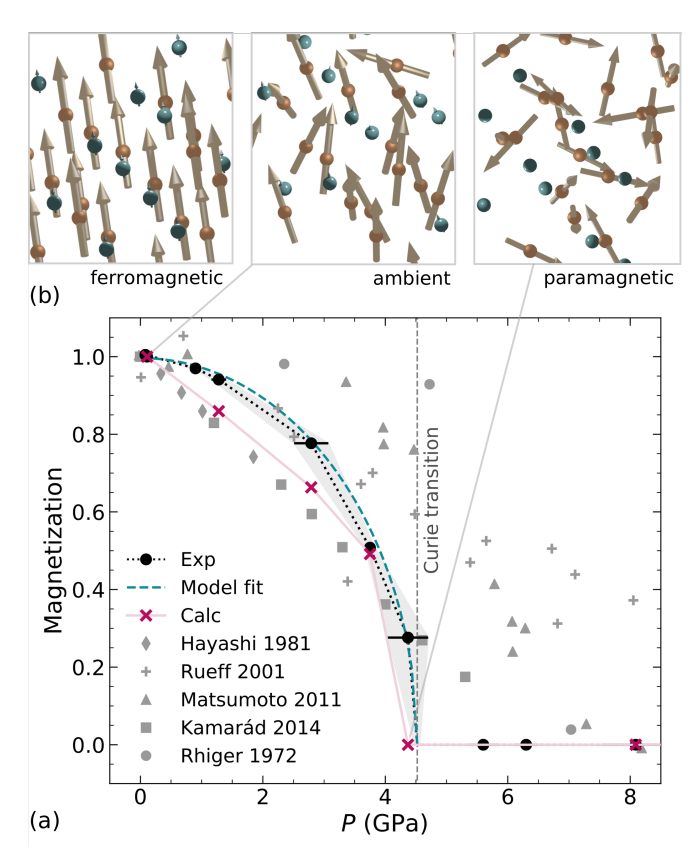


FIG. 3. Magnetization of Invar as a function of pressure. (a) Exp: normalized 57 Fe hyperfine magnetic field (HMF) vs. P from NFS experiments, with Model fit (full data set and fits are shown in Supplementary Figs. S2 and S3). Error bars show the standard deviation of the pressure inside the diamond anvil cells between two pressure probes near the sample, measured before and after each data collection. Calc: calculated M(P) as described in text. The calculated curve is shifted so the calculated equilibrium volume corresponds to the measured ambient volume. Gray symbols: Literature data from different M(P) measurements (references are labeled [33–37]). (b) Calculated spin configurations at the Fe (orange) and Ni (blue) atoms for the fully ordered ferromagnetic (0 K), ambient, and paramagnetic states. Arrow sizes are proportional to the calculated magnetic moments.

therefore, an important role in the Invar effect.

MAGNETIC ENTROPY

Figure 3a compares the calculations of normalized magnetization as a function of pressure to those from experiment and to data published in the literature. Starting near a ferromagnetic spin arrangement at ambient conditions, the magnetization decreases with pressure. The Curie transition from a ferromagnetic to a paramagnetic state occurs at a pressure of 4.6 GPa, as found by fitting a mean-field model to the measured data. Examples of the calculated magnetic spin configurations for the fully

ordered (ferromagnetic), ambient, and fully disordered (paramagnetic) conditions are shown in Fig. 3b. It is evident that most of the bulk magnetization originates at the Fe atoms (orange), with only a small contribution from Ni (blue).

We determined the magnetization M(P) from NFS measurements of the 57 Fe hyperfine magnetic field (HMF), which is proportional to the lattice magnetization at Fe atoms [38]. Although NFS spectra are sensitive only to 57 Fe atoms, prior studies [11, 13, 14] and our present calculations have shown that the magnetic moments of the Ni atoms are much smaller than those of the Fe atoms. Furthermore, studies have shown that the orientation of the Ni magnetic moments is less affected by pressure [11, 35]. The Ni atoms make only a small contribution to the entropy of magnetic disordering in Invar. At high pressures, above the Curie transition, the magnetization goes to zero in accordance with previous Mössbauer measurements [37] (details are explained with Supplementary Figs. S2 and S3).

We measured the heat capacity $C_P(T)$ of Invar by differential scanning calorimetry (DSC). The magnetic component, $C_{P,\text{mag}}(T)$, was found by subtracting the electronic contribution and the phonon heat capacity (calculated from the phonon DOS of Fig. 1) from the measured C_P , as shown in the Supplementary Fig. S4. The total change in magnetic entropy from ambient temperature to the Curie transition was obtained as $S_{\text{mag}}^{\Delta T} = \int_{300K}^{T_C} C_{P,\text{mag}}/T \, \mathrm{d}T = 0.11 \, k_{\text{B}}/\text{atom}$. It was used to calibrate the entropy change associated with the demagnetization of Fig. 3 from ambient pressure to the Curie transition. The pressure dependence of the magnetic entropy was determined as in [39], using a mean-field model with a spin disordering that corresponds to the decreasing magnetization M(P) of Fig. 3:

$$\Delta S_{\text{mag}}(P) = -\frac{S_{\text{mag}}^{\Delta T}}{2\ln 2} \left[\left(M(P) + 1 \right) \ln \left(\frac{M(P) + 1}{2} \right) + \left(1 - M(P) \right) \ln \left(\frac{1 - M(P)}{2} \right) \right]$$

This model does not include magnetic short-range order, so it is used only for the magnetic entropy below the Curie transition. Figure 4a compares the resulting change in magnetic entropy $\Delta S_{\text{mag}}(P)$ to the measured phonon entropy $S_{\text{ph}}(P)$.

THERMAL EXPANSION AND SPIN-PHONON COUPLING

The essence of the near-zero thermal expansion of Invar is the near-cancellation of contributions from phonons and magnetism in Eq. 4. Figure 4 shows how the experimental entropies of phonons and spins change with

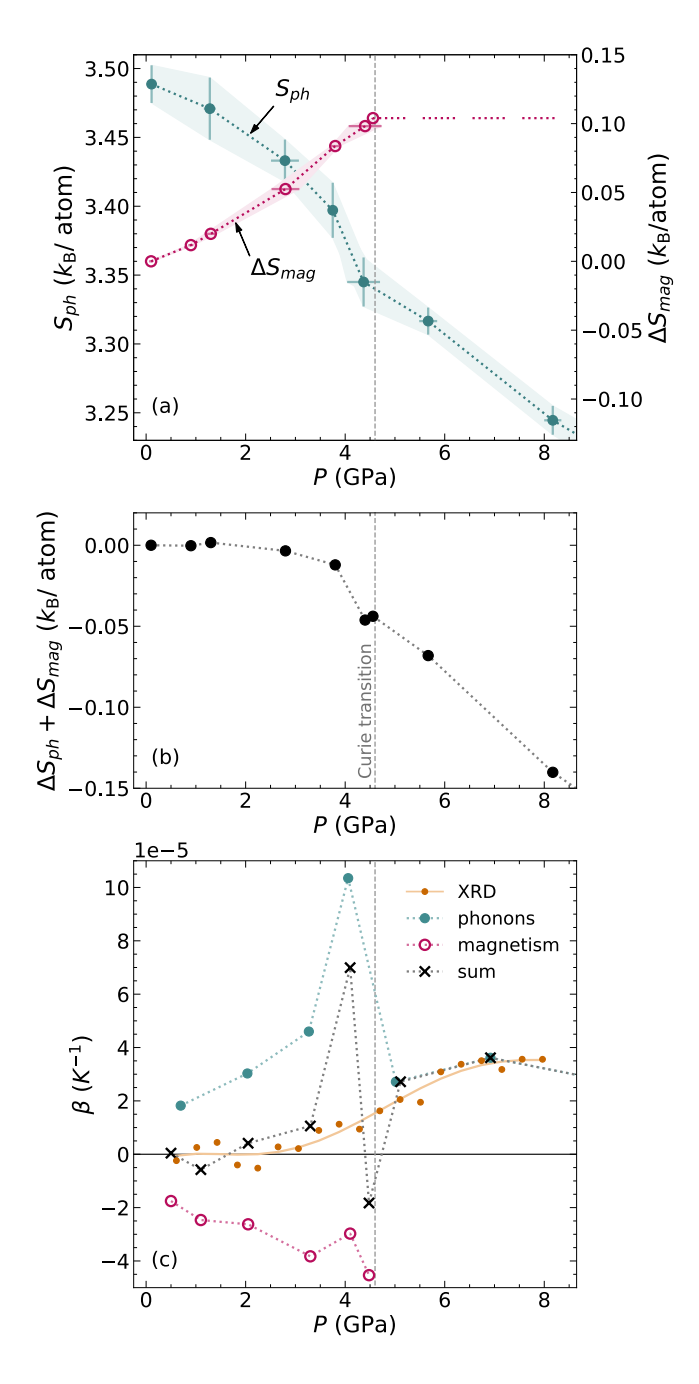


FIG. 4. Entropy contributions and thermal expansion. (a) Experimental phonon entropy $(S_{\rm ph}, \, \text{left axis})$ compared to experimental change in magnetic entropy $(\Delta S_{\rm mag}, \, \text{right axis})$ vs. P. The same scaling is used for the left and right axes. Error bars represent the standard deviation of the pressure inside the diamond anvil cell. The uncertainty of $S_{\rm ph}$ is from Fig. 2. (b) Entropy change by adding the changes in entropy from phonons and magnetism. (c) Volumetric thermal expansion coefficient β . Results from X-ray diffraction, XRD, (see Supplementary Fig. S1) are compared to individual contributions from phonons, and magnetic spins (calculated from entropies of panel a with Eq. 3) and their sum (from panel b).

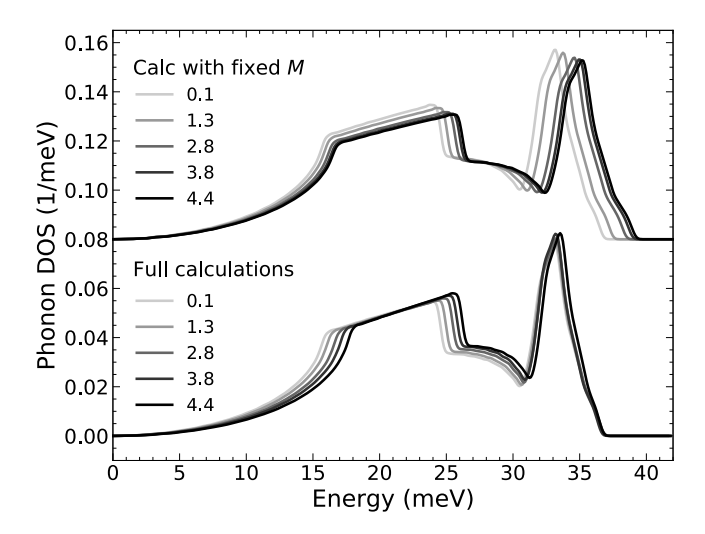


FIG. 5. Calculated phonon DOS below the Curie transition. Full calculations include a pressure dependent M that decreases with P, and calculations with fixed M, maintain its ambient value for all pressures. The pressures are labeled in GPa.

pressure. Their opposing changes give a nearly pressureindependent sum below 3 GPa as shown in Fig. 4b. This same pressure range coincides with the near-zero thermal expansion region measured by synchrotron X-ray diffraction, included in Fig. 4c. From 0 to 3 GPa the individual contributions to thermal expansion of Eq. 4 from phonons and magnetism both increase in magnitude. Their individual magnitudes rise from 2 to approximately $4 \times 10^{-5} \,\mathrm{K}^{-1}$, values even larger than the thermal expansion at higher pressures of $3.4 \times 10^{-5} \,\mathrm{K}^{-1}$. Since their signs are opposite, however, they cancel each other out, giving a near-zero total thermal expansion. At pressures above 3 GPa, the accurate cancellation is lost. The sum $\Delta S_{\rm ph} + \Delta S_{\rm mag}$ changes with P, and β becomes positive, even below the Curie transition at 4.6 GPa. At 8 GPa, a pressure well above the Curie transition, the thermal expansion of Fe₆₅Ni₃₅ is calculated with Eq. 4 to be about $\beta = 3 \times 10^{-5} \text{ K}^{-1}$, in agreement with the value of $3.4 \times 10^{-5} \text{ K}^{-1}$ measured by synchrotron X-ray diffraction.

The electronic entropy at 300 K was calculated ab initio from the electronic DOS. At ambient pressure, a small value of $9.5 \times 10^{-6} \, \mathrm{eV/K/atom}$ (0.11 $k_\mathrm{B}/\mathrm{atom}$) was obtained. Over the range of Invar behavior, the change in electronic entropy with P is about an order-of-magnitude smaller than changes in the phonon and magnetic entropies.

The spin disordering below the Curie transition causes a monotonic increase in the magnetic entropy. As described with Fig. 2, this magnetic disordering changes the phonon energies, altering the shape of $S_{\rm ph}(P)$ to counteract more precisely the pressure-dependence of the

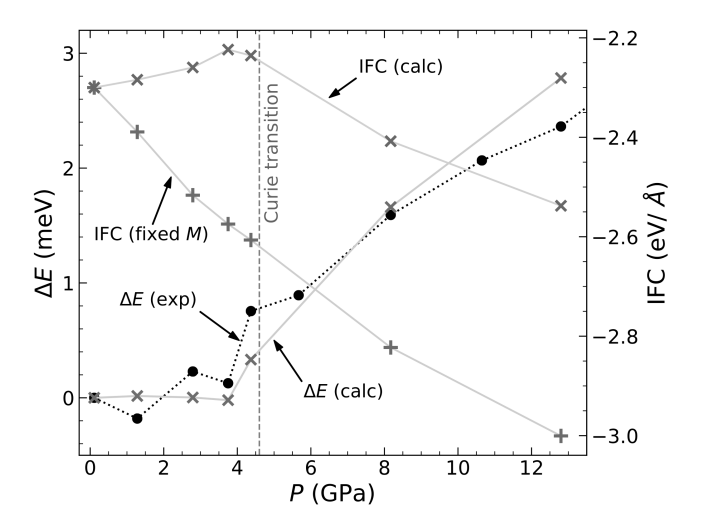


FIG. 6. Mean energy of longitudinal mode and longitudinal interatomic force constants. Left axis: Energy shift of high energy peak with pressure, ΔE , from longitudinal modes of the experimental and calculated phonon DOS of Fig. 1. The experimental energy shifts were obtained by fitting three Lorentzians to the phonon DOS of Fig. 1. Right axis: Bondstretching irreducible IFC (along the bond direction) vs pressure. IFC (calc): full calculation. IFC (fixed M): M fixed at ambient value.

magnetic entropy. Without the spin-phonon interactions, Fig. 2 shows that the phonon entropy would change approximately linearly with P, as given by a Grüneisen parameterization, for example. Such a linear decrease with P would not counteract so effectively the concave curve of magnetic entropy. The effect of magnetization on the phonon DOS is shown in Fig. 5, where the phonon DOS curves from full calculations are compared to calculations with a fixed magnetization. When M is fixed artificially, the entire phonon spectrum shifts to higher energies with P. The full calculations, in contrast, show that for pressures from 0 to 4 GPa, the position of the high-energy peak from longitudinal modes remains fixed in energy, as shown in detail in Fig. 6 (ΔE , left axis). This independence of pressure is unlike the smooth increase in phonon energies typical of the stiffening of chemical bonds with decreasing crystal volume (which is observed above the Curie transition). It suggests that the spin-phonon coupling serves to decrease the energy of the longitudinal modes with increasing P, counteracting the usual increase with P. We validated this interpretation with calculations where the volume was held fixed while the orientational disorder of the Fe and Ni magnetic moments in the supercell was artificially increased. These calculations confirmed that a decreasing magnetization shifts the high-energy peak in the phonon DOS monotonically to lower energies.

The fixed position of the peak from the longitudinal modes suppresses the change of phonon entropy at low pressure, shown in Fig. 4a. The observed decrease in entropy below the Curie transition comes from the upwards shift of the transverse modes (see Fig. 5), which reduces the available states at low energies where the Planck distribution of phonon occupancy ($n_{\varepsilon,T}$ in Eq. 5) is largest.

The spin-phonon coupling is also evident in the effect of magnetic disorder on the chemical bonding. The first-nearest-neighbor interatomic force constants (IFC) are also plotted against pressure in Fig. 6. This IFC is for stretching along the bond direction and dominates the behavior of longitudinal phonon modes. Below 3 GPa, the IFC is nearly constant with pressure, consistent with a minimal shift of the longitudinal peak in the phonon DOS. An abrupt change occurs near 4 GPa beyond which the IFC decreases monotonically, consistent with the observed upward shift of the longitudinal peak. When the magnetization is held constant for all pressures, the IFC simply strengthens monotonically, corresponding to a continuous upward shift of the longitudinal peak, contrary to the experimental behavior.

CONCLUSIONS

At room temperature, synchrotron X-ray diffraction showed that $Fe_{65}Ni_{35}$ Invar has near-zero thermal expansion from 0 to 3 GPa. Experimental determinations of spin and phonon entropies gave the individual components of thermal expansion from magnetism and atom vibrations. Both these contributions increase in magnitude with pressure up to the Curie transition at 4.6 GPa, but they have opposite signs. A spin-phonon interaction below $T_{\rm C}$ causes the pressure dependence of the phonon entropy to better oppose the nonlinear trend of the magnetic entropy with pressure. The most accurate cancellation of the phonon and spin contributions to thermal expansion occurs in the pressure range of the Invar effect, and this cancellation gives the Invar effect.

ACKNOWLEDGMENTS

This work was supported by the National Science Foundation under Grant No. 1904714 (S.H.L., P.G., C.M.B-C., C.N.S., B.F.). Work at Boston College was supported by the US Department of Energy (DOE), Office of Science, Basic Energy Sciences under award No. DE-SC0021071 (M.H., D.B.). O.H. acknowledges support from the Swedish Research Council (VR) program 2020-04630. M.H. and D.B. acknowledge the Boston College Linux clusters for computational resources and support. Calculations were also performed in part using MATLAB. This research used resources of the Advanced Photon Source, a U.S. Department of Energy (DOE) Office of Science User Facility operated for the DOE Office of Science by Argonne National Labora-

tory under Contract No. DE-AC02-06CH11357 (S.H.L., P.G., C.M.B-C., G.S., B.F.). HPCAT operations are supported by DOE-NNSA's Office of Experimental Sciences. Use of the COMPRES-GSECARS gas loading system was supported by COMPRES under NSF Cooperative Agreement EAR-1606856 and by GSECARS through NSF grant EAR-1634415 and DOE grant DE-FG02-94ER14466. This research also used resources at the Spallation Neutron Source, a DOE Office of Science User Facility operated by the Oak Ridge National Laboratory (S.H.L., C.M.B-C., B.F.). We thank David Rhiger for informing us of his disseration research, Prof. Chen Li for assistance with the pressure cells, and Prof. J. A. Kornfield for use of the DSC. We also acknowledge the help from the beamline scientists at the APS (E. Ercan Alp, Jiyong Zhao, Barbara Lavina and Michael Hu) and Douglas Abernathy at ORNL.

AUTHOR CONTRIBUTIONS

S.H.L. designed and performed the experiments, analyzed the data, and compiled the manuscript. M.H. performed and analyzed the calculations. P.G. and C.M.B-C. helped execute the beamline experiments at the APS. C.N.S. analyzed the neutron scattering data. The remote X-ray diffraction experiments were locally handled by G.S. O.H. developed and supervised the computational analyses. D.B. conceptualized and supervised the computational efforts. B.F. conceptualized and supervised the study. S.H.L., M.H., D.B. and B.F. wrote the manuscript, with contributions from all authors.

ADDITIONAL INFORMATION

Competing interests The authors declare no competing interests.

Correspondence and requests for materials should be addressed to S. H. Lohaus (lohaus.stefan@gmail.com) or B. Fultz (btf@caltech.edu).

FIGURE CAPTIONS

Fig. 1. Phonon DOS of Invar at different pressures as labeled. Experimental partial DOS curves measured by NRIXS (black curves) are compared to the calculated DOS (orange curves), both are normalized to 1. Error bars show the standard deviation of sequential NRIXS scans (on average, a total of 39,480 counts were recorded for each inelastic spectrum). At ambient conditions, the NRIXS measurement is in excellent agreement with the DOS measured by INS (blue markers).

Fig. 2. Phonon entropy of Invar as a function of pressure. The entropy, $S_{\rm ph}(P)$, was calculated with Eq. 5 us-

ing the experimental (Exp) and calculated (Calc) phonon density of states. Calc: full calculation using M(P) according to Fig. 3. Calc (fixed M): magnetization artificially fixed at the ambient value. Calculated curves are shifted so their volumes coincide with the experimental at ambient volume. Experimental error bars were propagated from the DOS errors and represent the standard deviation of sequential measurements. They were calculated using Eq. 5 from an ensemble of 200 DOS curves generated from the error bars of Fig. 1 by a Monte-Carlo method. The standard deviation in pressure was computed from two pressure probes (ruby spheres) inside the diamond anvil cell, measured before and after each spectrum (see Methods).

Fig. 3. Magnetization of Invar as a function of pressure. (a) Exp: normalized ⁵⁷Fe hyperfine magnetic field (HMF) vs. P from NFS experiments, with Model fit (full data set and fits are shown in Supplementary Figs. S2 and S3). Error bars show the standard deviation of the pressure inside the diamond anvil cells between two pressure probes near the sample, measured before and after each data collection. Calc: calculated M(P) as described in text. The calculated curve is shifted so the calculated equilibrium volume corresponds to the measured ambient volume. Gray symbols: Literature data from different M(P) measurements (references are labeled [33–37]). (b) Calculated spin configurations at the Fe (orange) and Ni (blue) atoms for the fully ordered ferromagnetic (0 K), ambient, and paramagnetic states. Arrow sizes are proportional to the calculated magnetic moments.

Fig. 4. Entropy contributions and thermal expansion. (a) Experimental phonon entropy $(S_{\rm ph},$ left axis) compared to experimental change in magnetic entropy $(\Delta S_{\rm mag},$ right axis) vs. P. The same scaling is used for the left and right axes. Error bars represent the standard deviation of the pressure inside the diamond anvil cell. The uncertainty of $S_{\rm ph}$ is from Fig. 2. (b) Entropy change by adding the changes in entropy from phonons and magnetism. (c) Volumetric thermal expansion coefficient β . Results from X-ray diffraction, XRD, (see Supplementary Fig. S1) are compared to individual contributions from phonons, and magnetic spins (calculated from entropies of panel a with Eq. 3) and their sum (from panel b).

Fig. 5. Calculated phonon DOS below the Curie transition. Full calculations include a pressure dependent M that decreases with P, and calculations with fixed M, maintain its ambient value for all pressures. The pressures are labeled in GPa.

Fig. 6. Mean energy of longitudinal mode and longitudinal interatomic force constants. Left axis: Energy shift of high energy peak with pressure, ΔE , from longitudinal modes of the experimental and calculated phonon DOS of Fig. 1. The experimental energy shifts were obtained by fitting three Lorentzians to the phonon DOS of Fig. 1. Right axis: Bond-stretching irreducible IFC (along the

bond direction) vs pressure. IFC (calc): full calculation. IFC (fixed M): M fixed at ambient value.

- Wasserman, E. F. Invar: moment-volume instabilities in transition metals and alloys, in *Ferromagnetic Materials*, Vol. 5, 237–322, North-Holland, Amsterdam (1990).
- [2] Guillaume, C. E. Recherches sur les aciers au nickel. Dilatations aux temperatures elevees; resistance electrique. CR Acad. Sci. 125, 235 (1897).
- [3] Guillame, C. E. Nobel Lecture in physics (1920). https://www.nobelprize.org/uploads/2018/06/guillaume-lecture.pdf
- [4] Kübler, J. Magnetic moments of ferromagnetic and antiferromagnetic bcc and fcc iron. Phys. Lett. A 81, 1 (1981).
- [5] Pinski, F. J., Staunton, J., Gyorffy, B. L., Johnson, D. D., Stocks, G. M. Ferromagnetism versus antiferromagnetism in face-centered-cubic iron. *Phys. Rev. Lett.* 56, 19 (1986).
- [6] Keune, W., Ezawa, T., Macedo, W. A. A., Glos, U. Schletz, K. P., Kirschbaum, U. Magneto-volume effects in γ-Fe ultrathin films and small particles. *Physica B* 161, 269-275 (1989).
- [7] Weiss, R. J. The origin of the 'Invar' Effect. Proc. Phys. Soc. 82, 281 (1963).
- [8] Moruzzi, V. L., Marcus, P. M., Schwarz, K., Mohn, P. Ferromagnetic phases of bcc and fcc Fe, Co, and Ni. Phys. Rev. B 34, 3 (1986).
- [9] Schröter, M., Ebert, H., Akai, H., Entel, P., Hoffmann, E., Reddy, G. G. First-principles investigations of atomic disorder effects on magnetic and structural instabilities in transition-metal alloys. *Phys. Rev. B* 52, 1 (1995).
- [10] Entel, P., Hoffmann, E., Mohn, P., Schwarz, K., Moruzzi, V. L. First-principles calculations of the instability leading to the Invar effect. *Phys. Rev. B* 47, 8706 (1993).
- [11] van Schilfgaarde, M., Abrikosov, I. A. and Johansson, B. Origin of the Invar effect in iron-nickel alloys. *Nature* 400, 46 (1999).
- [12] Ehn, A., Alling, B., Abrikosov, I. A. First-principles theory of the pressure-induced invar effect in FeNi alloys. *Phys. Rev. B* 107, 104422 (2023).
- [13] Abrikosov, I. A., Kissavos, A. E., Liot, F., Alling, B., Simak, S. I., Peil, O. and Ruban, A. V. Competition between magnetic structures in the Fe rich fcc FeNi alloys. Phys. Rev. B 76, 014434 (2007).
- [14] Ruban, A. V. First-principles modeling of the Invar effect in Fe_{0.65}Ni_{0.35} by the spin-wave method. *Phys. Rev. B* 95, 174432 (2017).
- [15] Wassermann, E. F., Acet, M., Entel, P., Pepperhoff, W. Basic Understanding of the Relations between Invar, Anti-Invar and Martensite in Fe-based Alloys. J. Magn. Soc. Jpn. 23, 385 (1999).
- [16] Crisan, V., Entel, P., Ebert, H., Akai, H., Johnson, D. D. and Staunton, J. B. Magnetochemical origin for Invar anomalies in iron-nickel alloys. *Phys. Rev. B* 66, 014416 (2002).
- [17] Nataf, L., Decremps, F., Gauthier, M. and Canny, B. High-pressure structural study of Fe₆₄Ni₃₆ and Fe₇₂Pt₂₈ Invar alloys at low-temperature. *Phys. Rev. B* 74, 184422 (2006).

- [18] Dubrovinsky, L., Dubrovinskaia, N., Abrikosov, I. A., Vennström, M., Westman, F., Carlson, S., van Schilfgaarde, M. and Johansson, B. Pressure-Induced Invar Effect in Fe-Ni Alloys. Phys. Rev. Lett. 86, 4851 (2001).
- [19] Kizaki, T., Miyai, N., Hino, N., Saita, H., Tateiwa, N., Ohta, H., Ito, H., Iwai, J. and Kim, D. J. A new theory of the Invar behavior considering the role of phonon. J. Magn. Magn. Mater. 140–144, 245 (1995).
- [20] Kim, D. S., Hellman, O., Herriman, J., Smith, H. L., Lin, J. Y. Y., Shulumba, N, Niedziela, J. L., Li, C. W., Abernathy, D. L. and Fultz, B. Nuclear quantum effect with pure anharmonicity and the anomalous thermal expansion of silicon. *PNAS* 115, 1992 (2018).
- [21] Adeagbo, W. A., Zayak, A. and Entel, P. First-principles study of lattice instabilities in ferromagnetic L1₂ Fe₃Ni: direct force constants method versus linear response. *Phase Transitions* 79, 853 (2006).
- [22] Ikeda, Y., Körmann, F., Dutta, B., Carreras, A., Seko, A., Neugebauer, J. and Tanaka I. Temperaturedependent phonon spectra of magnetic random solid solutions. *Npj Comput. Mater.* 4, (2018).
- [23] Gruner, M. E., Adeagbo, W. A., Zayak, A. T., Hucht, A., Entel, P. Lattice dynamics and structural stability of ordered Fe₃ Ni, Fe₃Pd and Fe₃Pt alloys using density functional theory. *Phys. Rev. B* 81, 064109 (2010).
- [24] Endoh, Y. Lattice dynamics in ferromagnetic invar alloys. J. Magn. Magn. Mater. 10, 177 (1979).
- [25] Maliszewski, E. and Bednarski, S. Lattice Dynamics of Fe_{0.65}Ni_{0.35} Classical Invar. *Phys. Status Solidi b*, 211, 621 (1999).
- [26] Heine, M., Hellman, O. and Broido, D. Effect of thermal lattice and magnetic disorder on phonons in bcc Fe: A first-principles study. *Phys. Rev. B* 100, 104304 (2019).
- [27] Heine, M., Hellman, O., and Broido, D. Theory of thermal properties of magnetic materials with unknown entropy. *Phys. Rev. Mater.* 6, 113805 (2022).
- [28] Sturhahn, W. CONUSS and PHOENIX: Evaluation of nuclear resonant scattering data. Hyperfine Interact. 125, 149 (2000).
- [29] Chumakov, A. I., Sturhahn, W. Experimental aspects of inelastic nuclear resonance scattering. *Hyperfine Interact*. 123, 781 (1999).
- [30] Hellman, O., Abrikosov, I. A. and Simak, S. I. Lattice dynamics of anharmonic solids from first principles. *Phys. Rev. B* 84, 180301(R) (2011).
- [31] Hellman, O., Abrikosov, I. A. and Simak, S. I. Temperature dependent effective potential method for accurate free energy calculations of solids. *Phys. Rev. B* 87, 104111 (2013).
- [32] Fultz, B. Phase Transitions in Materials, 2^{nd} ed. Cambridge University Press, Cambridge (2020).
- [33] Hayashi K. and Mori, N. Effects of pressure on magnetization of Fe-Ni and Fe-Pt invar alloys. Solid State Commun. 38, 1057 (1981).
- [34] Rueff, J. P., Shukla, A., Kaprolat, A., Krisch, M., Lorenzen, M., Sette, F. and Verbeni, R. Magnetism of Invaralloys under pressure examined by inelastic x-ray scattering. *Phys. Rev. B* **63**, 132409 (2001).
- [35] Matsumoto, K., Maruyama, H., Ishimatsu, N., Kawamura, N., Mizumaki, M., Irifune, T., Sumiya, H. Non-collinear Spin Structure in Fe–Ni Invar Alloy Probed by Magnetic EXAFS at High Pressure. J. Phys. Soc. Japan 80, 023709 (2011).
- [36] Kamarád, J., Míšek, M. and Arnold Z. Direct measure-

- ment of magnetization isotherms of Fe₆₄Ni₃₆ Invar alloy in a diamond anvil cell. *High Press. Res.* **34**, 365 (2014).
- [37] Rhiger, D. Mössbauer Experiments in Iron-Nickel Alloys at High Pressures. Ph.D. dissertation in physics, Univ. Washington, Seattle (1972).
- [38] Kobeissi, M. A. Mössbauer study of static and dynamic critical behavior in Fe. Phys. Rev. B 24, 5 (1981).
- [39] Lohaus, S. H., Johnson, M. B., Ahnn, P. F., Saunders, C. N., Smith, H. L., White, M. A. and Fultz, B. Thermodynamic stability and contributions to the Gibbs free energy of nanocrystalline Ni₃Fe. *Phys. Rev. Mater.* 4, 086002 (2020).
- [40] Hrubiak, R., Sinogeikin, S., Rod, E., Shen, G. The laser micro-machining system for diamond anvil cell experiments and general precision machining applications at the High Pressure Collaborative Access Team. Rev. Sci. Instrum. 86, 072202 (2015).
- [41] Sturhahn, W. Nuclear resonant spectroscopy. J. Phys. Condens. Matter 16, 497 (2004).
- [42] Arnold, O., et al. Mantid—Data analysis and visualization package for neutron scattering and μ SR experiments. Nucl. Instrum. Meth. A 764, 156 (2014).
- [43] Lin, J. Y. Y., Islam F. and Kresh, M. Multiphonon: Phonon Density of States tools for Inelastic Neutron Scattering Powder Data. J. Open Source Softw. 3, 440 (2018).
- [44] Moriya, T. Spin fluctuations in itinerant electron magnetism. Springer-Verlag, Berlin Heidelberg New York (1985).
- [45] Hubbard, J. The magnetism of iron. Phys. Rev. B 19, 2626 (1979).
- [46] Hasegawa, H. Single-site functional-integral approach to itinerant-electron ferromagnetism. J. Phys. Soc. Jpn. 46, 1504 (1979).
- [47] Hasegawa, H. Single-Site Spin Fluctuation Theory of Itinerant-Electron Systems with Narrow Bands. J. Phys. Soc. Jpn. 49, 178 (1980).
- [48] Zunger, A., Wei, S.-H., Ferreira, L. G. and Bernard, J. E. Special quasirandom structures. *Phys. Rev. Lett.* 65, 353 (1990).
- [49] Kresse, G. and Hafner, J. Efficient iterative schemes for ab initio total-energy calculations using a plane-wave basis set. *Phys. Rev. B* 48, 13115 (1993).
- [50] Kresse, G. and Furthmüller, J. Efficiency of ab-initio total energy calculations for metals and semiconductors using a plane-wave basis set. *Comput. Mater. Sci.* 6, 15 (1996).
- [51] Kresse, G. and Joubert, D. Efficient iterative schemes for ab initio total-energy calculations using a plane-wave basis set. *Phys. Rev. B* 54, 11169 (1996).
- [52] Kresse, G. and Joubert, D. Efficiency of ab-initio total energy calculations for metals and semiconductors using a plane-wave basis set. *Phys. Rev. B* 59, 1758 (1999).
- [53] Blöchl, P. E. Projector augmented-wave method. *Phys. Rev. B* 50, 17953 (1994).
- [54] Hobbs, D. Kresse, G. and Hafner, J. Fully unconstrained noncollinear magnetism within the projector augmentedwave method. *Phys. Rev. B* 62, 11556 (2000).
- [55] Perdew, J. P. Burke, K. and Ernzerhof, M. Generalized Gradient Approximation Made Simple. *Phys. Rev. Lett.* 77, 3865 (1996).

METHODS

Sample Preparation

The Fe $_{65}$ Ni $_{35}$ Invar materials were prepared by arcmelting Fe with high-purity Ni (99.99%) under an argon atmosphere with a titanium getter. NRIXS and NFS are sensitive only to the 57 Fe isotope, which has a natural abundance of 2.2%. To enhance the measured signal, alloys were enriched with 95.73% 57 Fe (from Isoflex). The arc-melted ingots were rolled into 10-15 μ m foils and annealed at 600°C for 15 h in vacuum-sealed quartz ampoules. Their fully fcc crystal structure was confirmed by X-ray diffractometry. Samples were cut into squares of approximately $50\times50~\mu$ m and loaded into the diamond anvil cells.

Diamond Anvil Cells (DACs)

Panoramic and symmetric-type DACs were used to achieve high pressures for the NRIXS, NFS, and XRD measurements. To ensure hydrostatic pressures at the sample, the DACs were loaded with helium as the pressure medium using the gas loading system at Sector 13 of the APS (GSECARS). Beryllium gaskets are used in the DACs to minimize the absorption of the X-ray signals emitted from the sample. Sample chambers were created by drilling holes in the Be gaskets with a laser micro-machining system at Sector 16 of the APS (HP-CAT) [40].

The pressure inside the sample chamber is determined by measuring the optical fluorescence spectra from ruby spheres placed near the sample. We used 2-3 ruby spheres in our DACs and acquired their fluorescence spectra before and after each NRIXS and NFS measurement. The pressure error bars of Figs. 2, 3 and 4 show the standard deviation of the central wavelengths of these spectra. The mean error was $\sigma_P = 0.26\,\mathrm{GPa}$.

$\begin{array}{c} {\rm Nuclear~Resonant~Inelastic~X-ray~Scattering}\\ {\rm (NRIXS)} \end{array}$

The phonon DOS of ⁵⁷Fe was measured by NRIXS at beamline 3 ID-D of the Advanced Photon Source at the Argonne National Laboratory. The incoherent inelastic spectra were acquired with three avalanche photodiode detectors positioned at the openings of the panoramic DACs, approximately perpendicular to the incident X-ray beam. Inelastic spectra were measured by scanning the energy of the incident beam around the nuclear resonance of ⁵⁷Fe at 14.413 keV. The high-resolution monochromator sets the energy resolution of the inelastic spectra at about 1.1 meV. The phonon partial DOS of ⁵⁷Fe was obtained by using the PHOENIX software

package [28] to remove the resonant elastic peak, subtract the background, and calculate the 1-phonon contribution. Error bars were obtained as the standard deviation of sequential energy scans. The data at 5.7, 8.2, and 10.7 GPa were collected in a separate experimental beamtime at the APS, with samples from the same material, but with an improved NRIXS signal, and hence smaller error bars. The strength of the NRIXS signal depends on the optimization of the optics (monochromators and focusing KB mirrors), and of the detectors at the synchrotron. Detectors placed slightly closer to the sample, without the use of windows between the DAC and detectors, and optimized optics can account for the better statistics of these data points.

Nuclear forward scattering (NFS)

NFS measurements were performed at beamline 3 ID-D of the APS. The spectra were acquired by tuning the high-resolution monochromator to the nuclear resonance of ⁵⁷Fe (14.413 keV) and measuring the time-dependent intensity modulations from interferences between emissions from different nuclear excited states to their ground states. The Supplementary Fig. S2 shows these modulation patterns imposed on the exponentially decaying signal. Interference indicates that nuclear energies are split due to the presence of a magnetic field at the nuclei (nuclear Zeeman splitting). These intensity modulation patterns were analyzed to obtain distributions of hyperfine magnetic fields (HMF) [41] using the CONUSS software package [28]. The HMF distribution at each pressure was approximated by two asymmetrized Gaussians, and fit to the experimental data with CONUSS. The mean of these distributions provided the data points in Fig. 3.

Inelastic Neutron Scattering (INS)

INS measurements were performed at ambient conditions using the time-of-flight Wide Angular-Range Chopper Spectrometer (ARCS) at the Spallation Neutron Source of the Oak Ridge National Laboratory. A plate of Fe-36%Ni Invar with 1 mm thickness was suspended at a 45° angle with respect to the incident neutron beam with an energy of 60 meV. No background subtraction was necessary. The data were reduced to a phonon DOS after multiphonon scattering correction using Mantid and the Multiphonon package [42, 43].

X-ray Diffraction (XRD)

X-ray diffraction patterns were collected at beamline 16-BMD (HPCAT) of the Advanced Photon Source. The samples were loaded into symmetric-type DACs, which

were placed in a heating block, enabling measurements at room temperature (295 K) and 390 K. We fitted Gaussians to determine the position of the measured diffraction peaks and track how they change with pressure and temperature. The (111) diffraction gave the strongest signal and most reliable fits, so the lattice parameters shown in the Supplementary Fig. S1 were determined from these peaks. By quantifying the change of the lattice parameter between both temperatures, we determined the pressure dependence of the thermal expansion.

Differential Scanning Calorimetry (DSC)

We measured the heat capacity of $Fe_{65}Ni_{35}$ using a differential scanning calorimeter (Perkin-Elmer DSC 7). The samples were placed in aluminum crucibles and were measured under a constant flow of nitrogen gas. The differential heat flow to the Invar sample was compared to a reference sapphire material while heating both materials from RT to $873\,\mathrm{K}$. The instrument baseline, measured with empty crucibles, was subtracted from the differential signal. To minimize effects of a changing baseline, we measured each sample three times and performed empty measurements before and after each run. The measured heat capacity and its contributions from phonons, spins, and electrons are shown in the Supplementary Fig. S4.

Computational

The pressure dependent phonon DOS and the phonon contributions to the entropy were calculated with a method that includes explicitly the temperature and pressure dependence of the phonon and spin subsystems, and the coupling between them. For phonons, the TDEP [30, 31] Hamiltonian is

$$H_{\text{TDEP}} = U_0 + \sum_{i,\alpha} \frac{p_{i,\alpha}^2}{2M_i} + \frac{1}{2} \sum_{i,j,\alpha,\beta} \Phi_{i,j}^{\alpha,\beta} u_{i,\alpha} u_{j,\beta} , \quad (7)$$

where $p_{i,\alpha}$ is momentum and $u_{i,\alpha}$ is the displacement from equilibrium of the i^{th} atom in the α^{th} Cartesian direction, and the $\Phi_{i,j}^{\alpha,\beta}$ are effective interatomic force constants (IFCs) that include effects of chemical and thermal disorder, as well as spin-phonon coupling. The U_0 varies with temperature and volume.

The modern theoretic treatment of magnetism in a material depends on the degree to which the electrons are treated as localized in real space (fixed-length local magnetic moments with orientational disorder) vs localized in reciprocal space (itinerant magnetism where magnetization per atom varies due to electron spin-flip excitations). A material may lie anywhere between these two limiting cases; for instance, weakly ferromagnetic metals, with

low $T_{\rm C}$, lie in the intermediate region where magnetization is degraded by thermally-excited long-wavelength spin fluctuations. Another intermediate case is that of metals with intermediate $T_{\rm C}$, which are treated with variable-length local magnetic moments possessing orientational disorder [44]. The disordered local moments picture for finite-temperature itinerant electron systems gives a microscopic mechanism of how such thermallydisordered local moments may arise in itinerant electron systems [45–47]. This is the picture we adopt for Invar, assigning thermal disorder as described in the text. When spin-lattice coupling is included in the Hamiltonian, the electron spins become coupled to atomic positions, whereby the spin configurations may affect the interatomic forces and, conversely, the atomic positions may affect spin energies. Such effects are captured in our approach within the DFT calculation of each spinlattice microstate. When magnon quasiparticles are welldefined, this spin-lattice coupling may be treated perturbatively in the context of magnon-phonon coupling. Our renormalization approach is non-perturbative and so does not rely on the existence of well-defined magnons, so we use the more general term, spin-lattice coupling.

Procedurally, a supercell of Fe and Ni atoms is first constructed with atom arrangements from the special quasi-random structure (SQS) method [48]. Thermal atom displacements are imposed from phonons calculated by TDEP. (Initial guesses for IFCs were obtained from a single-parameter model adjusted to yield a maximum phonon energy of approximately 9 THz under ambient conditions.) Calculations were performed in the canonical ensemble at fixed volumes. The experimental pressures were converted to volumes for theory calculations using the measured lattice constant vs. pressure data, shifted in volume such that ambient pressure corresponds to the theory zero-pressure volume.

For each pressure (volume), snapshots of atomic displacements and spin orientations were generated. Incorporating only the spin orientations consistent with the measured magnetization, as described below, ensures that these snapshots represent the thermodynamically relevant microstates of the system. First principles calculations of the force on each atom in each supercell snapshot are then performed within the framework of Density Functional Theory (DFT) using the Vienna Abinitio Simulation Package (VASP) [49–52]. Spin-orbit coupling was included and fully non-collinear magnetic moment directions were constrained according to the spin-lattice snapshots. The projector augmented-wave method was employed [53, 54], the the exchange correlation was treated with the generalized gradient approximation parameterized by Perdew, Burke, and Ernzerhof [55]. In TDEP the effective IFCs are calculated using a least-squares optimization that best reproduces the DFTcalculated forces in the ensemble of supercells at RT. Phonon modes are then computed from these IFCs by

diagonalizing the dynamical matrix. These renormalized phonon modes are used to generate a new set of thermodynamically relevant snapshots, as described in Ref. [26], and the procedure is repeated until self-consistency is achieved.

Over the range of pressures considered in the experiments, sets of magnetic microstates are generated at the corresponding volumes with different magnetic moment orientations on the Fe and Ni atoms in the supercell. Each configuration defines a different order parameter, M/m, where M is the average magnetization per atom in the supercell, and m is the corresponding average magnitude of the local magnetic moment. For each macroscopic order parameter a set of inequivalent quasirandom structures that correspond to the macroscopic state are generated [48]. Due to the finite size of the sets of supercell configurations, a residual M/m of about 0.2 was present in the fully-disordered (nominal M/m=0) calculations. This is not expected to be a problem because for larger pressures, the calculated phonon modes are relatively insensitive to variations in the amount of magnetic disorder for small values of M/m. Sets of different

magnetic supercell configurations are generated for several different order parameters for each volume, defining a grid in M/m versus volume. The path through this space of M/m vs V gives an M(V) that is chosen to best match the measured magnetization, phonon DOS, and phonon entropy curves as a function of pressure. As part of this optimization procedure, an ambient pressure lattice constant of 3.573 Å was taken, which is within 1% of the measured value.

Data availability

All relevant data from experiments and calculations are available at https://doi.org/10.5281/zenodo.7987363.

Code Availability

The computer code used to generate numerical results is based on VASP and TDEP, both of which are publicly available. The formulations and algorithms necessary to reproduce the theory results of this study are described in the Methods section and in Ref. [27].